

Properties of Hydrated Excess Protons near Phospholipid Bilayers

Takefumi Yamashita and Gregory A. Voth*

Center of Biophysical Modeling and Simulation and Department of Chemistry, University of Utah,
315 South 1400 East, Room 2020, Salt Lake City, Utah 84112-0850

Received: September 10, 2009; Revised Manuscript Received: October 21, 2009

The behavior of the hydrated excess proton near different lipid membranes is studied with the third generation of the multistate empirical valence bond (MS-EVB3) model [Wu, Y. J.; Chen, H. N.; Wang, F.; Paesani, F.; Voth, G. A. *J. Phys. Chem. B* **2008**, *112*, 467]. Dioleoylphosphatidylcholine (DOPC), dioleoylphosphatidylethanolamine (DOPE), and dioleoylphosphatidylglycerol (DOPG) are selected as example lipids. In spite of the differences of the head groups, the molecular dynamics simulations show that all the lipid membranes have a proton-collecting antenna effect with no free energy barrier between the bulk water and interface regions. By comparison with classical hydronium model simulations, it is found that an appropriate description of proton Grotthuss shuttling and associated charge defect delocalization are necessary to obtain the correct free energy profile for the hydrated excess proton. In addition, nanosecond time scale sampling is essential to evaluate the free energy profiles, because certain slow motions are needed to stabilize the excess proton in the deep membrane interface region. It is also found that the lateral diffusion coefficients are 1 order of magnitude smaller in the interface region than in bulk water for all the lipids. These coefficients are almost the same as those of the lipid head groups. Finally, since the lipid phosphates may possibly be protonated due to the proton antenna effect of the membrane, phosphate group protonation is investigated and discussed within the MS-EVB framework.

1. Introduction

Proton transport is an important and challenging issue in both molecular biology and physical chemistry. In the field of physical chemistry, behavior of the excess proton near hydrophobic and hydrophilic interfaces^{1–21} has received considerable attention since the discovery of the amphiphilic nature of the hydronium,¹ and the phospholipid membrane is one example of the hydrophilic surfaces.^{19–21} From the viewpoint of biological energy conversion, the lipid membrane may have a more active role in the proton translocation than was previously considered.^{22–24} In the process of ATP production, the protons are pumped by several proton-transporting proteins (e.g., cytochrome *c* oxidase) and transferred along the lipid membrane to ATP synthase, which produces ATP by using the proton-motive force. It has been speculated that this two-dimensional proton transport along the membrane may be more efficient than the proton diffusing through the bulk water phase.

To clarify the role of the membrane in proton transport, many experiments have been carried out. For example, Heberle et al.²⁵ showed that protons travel along the membrane surface extensively by using a light-triggered experiment with purple membrane. In a similar experiment, Alexiev et al.²⁶ suggested that the proton diffusion coefficient along the membrane surface is higher than 0.3 Å²/ps. On a pure diphytanoylphosphatidylcholine (DPhPC) membrane, the proton diffusion coefficient was estimated to be 0.58 Å²/ps, which is slightly smaller than the value of the proton diffusion coefficient in bulk water.²⁷ More recently, Brändén et al.²⁸ carried out a fluorescence correlation spectroscopy experiment for the dioleoylphosphatidylglycerol (DOPG) liposome, finding that the membrane is an effective proton-collecting antenna. However, they suggested the proton

diffusion coefficient on the surface is about 0.002 Å²/ps, which is 2 orders of magnitude smaller than the previous experimental values.^{26,27}

Although these experiments point to the active role of the lipid membrane, a complete molecular scale understanding of the membrane effect on hydrated protons has not yet been achieved. Atomistic molecular dynamics (MD) simulation can be a useful and effective tool to obtain such molecular information, but such simulations of the proton–membrane interaction are very limited. This is because conventional classical empirical force fields cannot describe the bond alternation associated with the Grotthuss proton shuttling mechanism. Although ab initio methods can in principle describe such effects, the computational cost becomes very high and therefore statistically converged results for large enough systems are difficult to obtain. As an alternative, the multistate empirical valence bond (MS-EVB) method^{29–33} requires much lower computational cost than ab initio methods but can still accurately describe the bond alternation and Grotthuss shuttling behavior.

In fact, by using the MS-EVB method, Smondyrev and Voth¹⁹ were able to investigate the hydrated excess proton near the dimyristoylphosphatidylcholine (DMPC) lipid bilayer. The calculated potential of mean force (PMF) showed that the free energy of the excess proton is 0.7 kcal/mol lower in the head group layer of the membrane than in the bulk water region. Tepper and Voth²⁰ subsequently applied the umbrella sampling method to calculate the PMF. Although the free energy minimum was found to be deeper (2 ± 0.5 kcal/mol) in this PMF, the features of the PMF curves were similar and no high barriers were found. However, these PMF curves are completely different from the PMF for the dilauroylphosphatidylethanolamine (DLPE) membrane calculated by Zahn and Brickmann.³⁴ In the latter simulations, the excess proton in the head group region was found to be unstable compared to the bulk water

* Corresponding author. Phone: (801) 581-7272. Fax: (801) 581-4353.
E-mail: voth@chemistry.utah.edu.

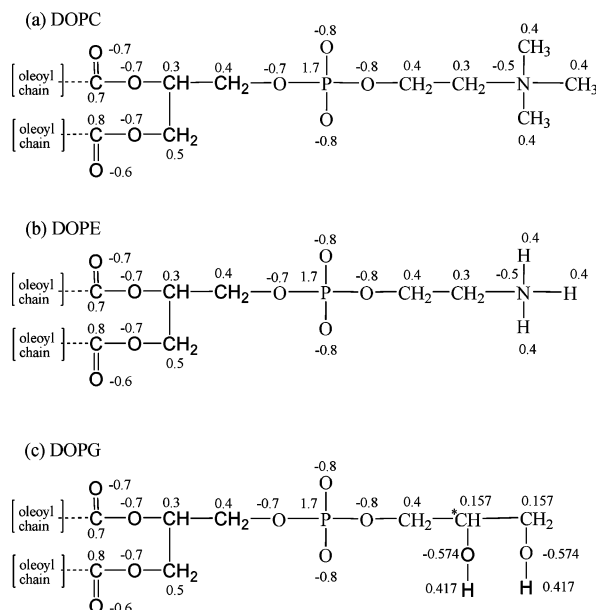


Figure 1. Lipid structures of (a) DOPC, (b) DOPE, and (c) DOPG. The numbers denote the on-site charge values. The asterisk indicates a chiral carbon atom.

region, and a 20 kcal/mol barrier was predicted for the proton transfer from the bulk water region to the membrane interface. As discussed in ref 19, however, it is difficult to compare the results for DMPC and DLPE, because the force field models and the simulation conditions are different.

The main purpose of this paper is to clarify how the lipid head group species affects the hydrated proton behavior from a molecular viewpoint. Based on a common force field model and simulation method, the statistical and dynamic properties are calculated and analyzed in detail. The DOPG membrane used in the experiments of Brändén et al.,²⁸ the dioleoylphosphatidylethanolamine (DOPE) membrane, and the dioleoylphosphatidylcholine (DOPC) membrane are systematically studied. The tail groups of the three lipids consist of the same oleoyl chains, whereas the head group of DOPG is anionic while those of DOPC and DOPE are zwitterionic. Replacing the head group species changes not only the charge distribution but also the membrane structural properties such as the average area per lipid. It is possible that these changes could affect the behavior of the hydrated excess proton near the bilayer both directly and indirectly. Finally, the effect of protonating the phosphate group is briefly discussed. The protonation of the phosphate group is usually not addressed because its pK_a value is quite low. However, if the lipid membrane collects the proton very efficiently, the pH at the surface will decrease considerably, and therefore the possibility of lipid protonation should at least be considered.

2. Force Fields and System Parameters

In this paper, DOPC, DOPE, and DOPG lipid bilayers are studied. These lipids are depicted in Figure 1. Each bilayer consists of 64 lipid molecules, 1568 water molecules (24.5 waters/lipid), and one excess proton. Since DOPG is an anionic lipid, 64 Na^+ ions are added as counterions for that system. Note that the same numbers of D-DOPG and L-DOPG lipids are included in each layer and thus the calculated DOPG bilayer has neutral chirality.³⁵

The hydrated excess proton behavior is described in terms of the latest version of the MS-EVB model, denoted MS-

EVB3.³¹ In the MS-EVB model,^{32,33} the Hamiltonian is represented by a dynamic basis set of the EVB states, each of which corresponds to a specific bonding topology of a hydronium cation and water molecules. Thus, the MS-EVB Hamiltonian can be written as

$$\mathbf{H} = \mathbf{H}_0 + \mathbf{V} \quad (1)$$

where the classical Hamiltonian, \mathbf{H}_0 , is a diagonal matrix whose elements are described by the classical force field of the hydronium and water molecules in different states corresponding to different bonding topologies. The force field of the water molecules is described in terms of the SPC/Fw model,³⁶ which can accurately reproduce numerous important water properties. The second term in eq 1, \mathbf{V} , is a characteristic feature of the MS-EVB model. These off-diagonal elements cause the mixing of the EVB states and thus allow Grotthuss shuttling to occur via dynamic rearrangements of the bonding topology. The MS-EVB3 model is parametrized based on ab initio potential energy calculations of various protonated water clusters as well as empirical data for the underlying water potential.

The diagonalization of the EVB Hamiltonian, \mathbf{H} , defines the ground-state eigenenergy and eigenvector at each MD time step, and the forces are calculated from the Hellman–Feynman theorem

$$F_{i\alpha} = -\left\langle \Psi_g \left| \frac{\partial \mathbf{H}}{\partial r_{i\alpha}} \right| \Psi_g \right\rangle = -\sum_{n=1}^{N_{\text{EVB}}} \sum_{m=1}^{N_{\text{EVB}}} c_n c_m \frac{\partial h_{nm}}{\partial r_{i\alpha}} \quad (2)$$

where h_{nm} is an element of the EVB Hamiltonian matrix, $r_{i\alpha}$ is the coordinate of particle i in the direction α ($=x,y,z$), and c_n is the amplitude of the EVB state $|n\rangle$. As the position of the “excess proton” is an ill-defined concept due to the delocalized nature of the excess protonic charge defect, the center of excess charge (CEC) is used as a coordinate of the charge defect.^{32,33} The coordinate of the CEC in the direction α is given by

$$r_{\alpha}^{\text{CEC}} = \sum_{n=1}^{N_{\text{EVB}}} c_n^2 r_{n\alpha}^{\text{COC}} \quad (3)$$

where $r_{n\alpha}^{\text{COC}}$ is the center of charge (COC) of the hydronium in EVB state $|n\rangle$.

The lipid force fields are all based on the dipalmitoylphosphatidylcholine (DPPC) force field, developed by Berger, Edholm, and Jähnig.³⁷ The cis double bond in the oleoyl chain is taken from GROMOS96.³⁸ The parameters for the glycerol part in DOPG and the ammonium part in DOPE are modeled via 1,2-propanediol and lysine, respectively.^{35,39} Small Lennard-Jones potentials ($\epsilon = 0.4 \times 10^{-4}$ kcal/mol and $\sigma = 0.0$ Å), which are identical to that of hydronium hydrogen, are put on the explicit hydrogen atoms of lipids. For the sodium ions, the standard GROMOS96 force field is used.³⁸

All the MS-EVB simulations were performed in the constant NVT ensemble. MD calculations were performed with the DL_POLY2.15 program,⁴⁰ which was adapted for the MS-EVB3 model. Temperature was controlled to be $T = 308$ K with a Nose–Hoover thermostat⁴¹ with a thermostat relaxation time of 0.2 ps. The simulation box sizes were determined by the 50 ns constant NpT MD equilibration without the excess proton. In the first 46 ns, all the OH bond lengths and HOH angles of waters were fixed and the time step was set to be 2 fs. A

Berendsen thermostat and a semi-isotropic barostat were used with relaxation constants of 0.1 and 1 ps, respectively.⁴² In the last 4 ns, all the bonds and angles were flexible and the time step was 1 fs. The relaxation constant of the Berendsen barostat was increased to 100 ps in order to decrease the box size deviation. The area/lipid values of DOPC, DOPE, and DOPG were evaluated to be 64.5, 51.9, and 52.6 Å², respectively. These values agree with the calculated and experimental values reported previously.^{35,39,43} After equilibration, one excess proton was added to the system in the bulk water. In this paper, the *z* coordinate of each membrane system was set to be perpendicular to the membrane surface and the center of the lipid bilayer was set to be *z* = 0.

3. Characterization of the Membrane Surfaces

Before giving the results of the hydrated excess proton behavior near the lipid bilayers, the three lipid membranes are characterized in this section. Figure 2a–c shows the number density profiles calculated from the last 4 ns of the equilibration trajectories. The distribution of P, the phosphorus of the phosphate group, in the DOPC membrane is wider than that in the DOPE and DOPG membranes. The cationic sites of all three systems are distributed around the phosphate group. The distribution of choline (N site) is shifted toward the bulk water region. This may be due to the large volume of the choline group, which prevents its mobility into the deep interface region. In contrast, most Na⁺ ions are located at the deep interface region, which is surrounded by carbonyl and phosphate oxygen sites.

To characterize the hydrophilic interface in more detail, the electrostatic potentials were calculated through the double integral of the charge density $\rho_{\text{ch}}(z)$ ⁴⁴

$$\Delta\Psi(z) = \Psi(z) - \Psi(z_0) = - \int_{z_0}^z \int_{z_0}^{z'} \rho_{\text{ch}}(z'') dz'' dz' / 2\epsilon_0 \quad (4)$$

where z_0 is the center of the bilayer. The results are shown in Figure 2d. For the DOPC membrane, the electrostatic potential is -0.62 ± 0.01 V in the bulk water region and 0.19 ± 0.02 V at the location of the phosphate groups ($z = 20$ Å). These features are consistent with the previous simulation results.^{35,44,45} The experimental values for the bulk water regime are also in the same order.^{46,47} For DOPG, the $\Delta\Psi$ at the bulk water regime (-0.56 ± 0.04 V) is slightly higher than for DOPC. This tendency agrees with the previous simulation result.³⁵ For DOPE, the $\Delta\Psi$ at the bulk water regime (-0.74 ± 0.03 V) is lower than for the other two lipids, and has a deeper minimum around $z = 17$ Å, where the carbonyl groups are located.

The electrostatic potential calculated here includes the effect of water orientation near the membrane interface. Without water charges, the $\Delta\Psi(z \approx 30)$ is increased to 5.44 ± 0.09 , 2.43 ± 0.02 , and 4.37 ± 0.58 V for DOPC, DOPE, and DOPG, respectively (see Figure S1a in the Supporting Information). This indicates that the water near the lipid membrane is highly ordered and thereby decreases the electrostatic potential. It is possible that this behavior of water affects the hydrated proton solvation and transport near the membrane. The $\Delta\Psi(z \approx 30)$ value without water is much smaller for DOPE than for the other lipids, though the total $\Delta\Psi(z \approx 30)$ values are almost the same. This suggests that the water near the DOPE membrane is less ordered and the excess proton behavior near the DOPE membrane may be different from that near the DOPC membrane.

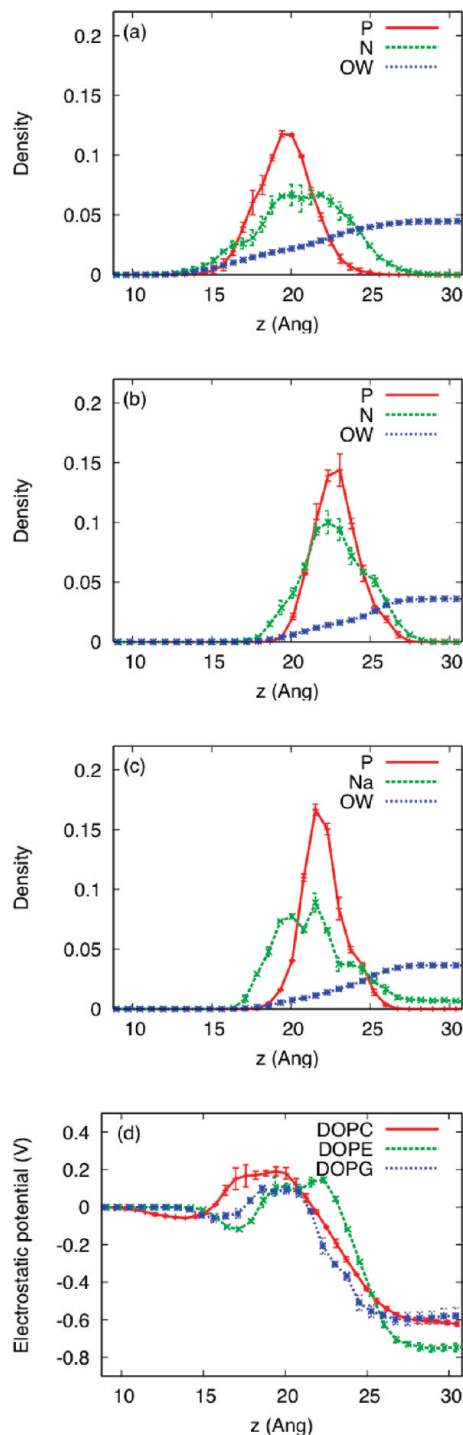


Figure 2. Number density profiles as functions of the normal direction coordinate *z* for (a) DOPC, (b) DOPE, and (c) DOPG membranes. P and OW are the phosphorus of the anionic phosphate group and the oxygen in water, respectively. N is the center atom of cationic choline or amine group. Na⁺ is the positive counterion in the DOPG membrane system. (d) Electrostatic potentials for DOPC, DOPE, and DOPG.

The value of $\Delta\Psi$ is an important quantity for the interaction between the ion and lipid membrane. In fact, it can explain that anions transport across the hydrophobic regime of the lipid bilayer much faster than cations.⁴⁸ As shown in Figure 2d, this analysis seems to indicate that cations would be unstable at the membrane interface, in contrast to experiments that show the proton-collecting antenna effect of the lipid membrane.²⁸ This discrepancy can be attributed to the following two effects. First, the analysis assumes a mean field interaction, but local interac-

tions can be important at rough surfaces (see Figure S1b–d in the Supporting Information). Second, the analysis does not consider the effect of the molecular reorganization. When the ion approaches the membrane surface, lipid head groups and waters near the membrane will reorient to stabilize the ion. These nontrivial molecular-scale effects frame the discussion of the explicit proton simulations described below.

4. Potentials of Mean Force and Unbiased MS-EVB Simulations

4.1. DOPC Membrane. The PMF for the excess proton was first calculated as a function of the z coordinate of the CEC using the umbrella sampling method. The harmonic umbrella potentials for the CEC²⁰ were used with a spring constant of 5 kcal/mol/Å² and the center positions of $z = 30, 29, 28, \dots$. The first MD trajectory was calculated from the bulk water region for 100 ps, and the final configuration of that trajectory was sequentially used as an initial configuration in the next window. In each window, a subsequent 400 ps trajectory was calculated to estimate the PMF. From the biased trajectories, the PMF curve was reconstructed through the weighted histogram analysis method (WHAM).^{49–51} This is similar to the procedure used by Tepper and Voth,²⁰ where a 250 ps trajectory was calculated in each window for the DMPC bilayer. The resultant PMF curve is consistent with the PMF curve calculated by Tepper and Voth.²⁰ The depth of the first minimum is 2 kcal/mol and the second stable state can be found in the deeper interface region, as shown by the green curve in Figure 3a.

Additionally, a 5 ns unbiased MD simulation was performed. In this simulation, the hydrated excess proton equilibrated and remained stable around the deep interface region ($z = 15$ Å). The difference between the implied behavior from the PMF calculated by umbrella sampling with 400 ps trajectories per window and the behavior of the 5 ns trajectory implies that subnanosecond equilibration in the umbrella sampling windows is not sufficient and therefore at least nanosecond simulations are required. Indeed, Tepper and Voth²¹ have discussed the pitfalls of subnanosecond sampling for several kinds of ions near the DMPC membrane. This is a result of the slow motion in the deep interface region, which will be discussed later.

To take the nanosecond relaxation behavior into account, the results of the last 4 ns of the unbiased trajectory and the 400 ps biased trajectories were combined through the WHAM procedure^{49,50} to reconstruct the PMF. This combination means that the data points are sampled by the long unbiased MD trajectory around the stable interface region where the motion is slow, while the biased MD samples the data points around the bulk water region where the free energy is high but the motion is faster. Thus, as shown by the red curve in Figure 3a, the resultant PMF curve is significantly changed by including the unbiased MD sampling data. The deep interface region ($z = 15$ Å) is stabilized and becomes the global minimum, while this region is metastable in the subnanosecond umbrella sampling calculations. The depth of the global minimum is 5 kcal/mol measured from the bulk water regime. This minimum is 2 times deeper than the minimum calculated by the short time umbrella sampling as seen in Figure 3a.

To characterize the solvation structure of the excess proton, the distribution of the EVB state population, $|c_0|^2$,^{29–31} was calculated as a function of z . First, the MD trajectories were combined with two-dimensional WHAM^{49,50} and the two-dimensional distribution was obtained as a function of the z coordinate of CEC and EVB state population $|c_0|^2$. Next, the two-dimensional distribution function was normalized for each

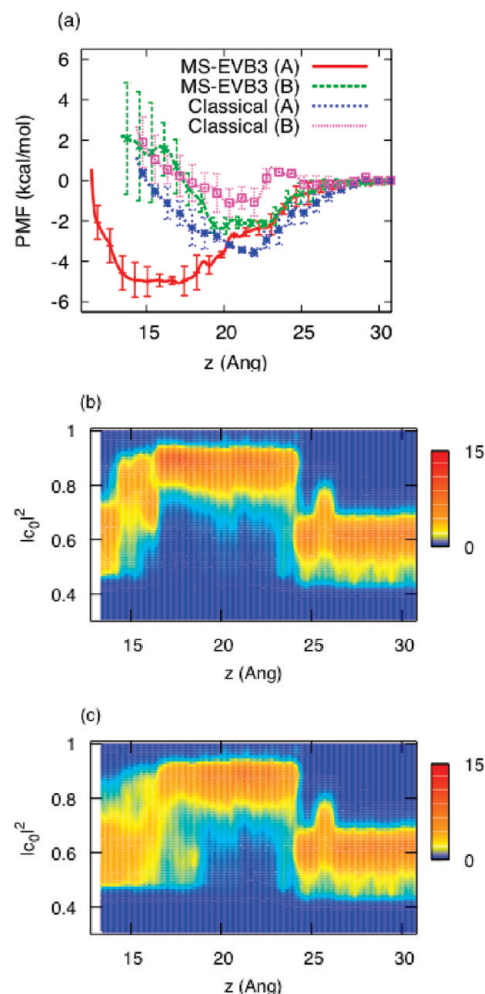


Figure 3. (a) PMF curves with respect to the z coordinate of CEC for DOPC membrane. Curve A is calculated from both biased and unbiased MD simulations, whereas curve B is calculated from the biased MD alone. (b) Distribution of the largest MS-EVB state population calculated from the biased MD alone. (c) Distribution of the largest MS-EVB state population calculated from the biased and unbiased MD.

z value. Figure 3b and 3c show the distribution functions that are calculated from the short biased umbrella sampling MD simulations alone and the longer unbiased plus biased MD simulation, respectively. In the bulk water region and shallow interface region, the two distributions are very similar. In the bulk water region, the EVB state population, $|c_0|^2$, is distributed around 0.6, which agrees with the result for the hydrated proton in bulk water.^{29–31} At $z = 26$ Å, the EVB state population is slightly increased by the electrostatic interaction from the membrane. A large jump in the $|c_0|^2$ distribution can be seen at $z = 24$ Å, which corresponds to the excess proton charge defect becoming more localized onto a hydronium-like structure so as to enhance the electrostatic interaction between the excess charge and the anionic sites of the lipids.

In the deep interface region ($z \leq 18$ Å), the excess proton charge defect becomes more delocalized, and a distorted Zundel cation, H_5O_2^+ , is more extensively formed. This structure does not correspond to the traditional symmetric Zundel cation, but this delocalized structure is Zundel-like because the excess charge is primarily distributed across only two EVB states. (The sum of the first and the second largest EVB populations, $|c_0|^2 + |c_1|^2$, is larger than 0.9.) This structure is primarily due to the Zundel-like cation's ability to bridge the negative lipid head

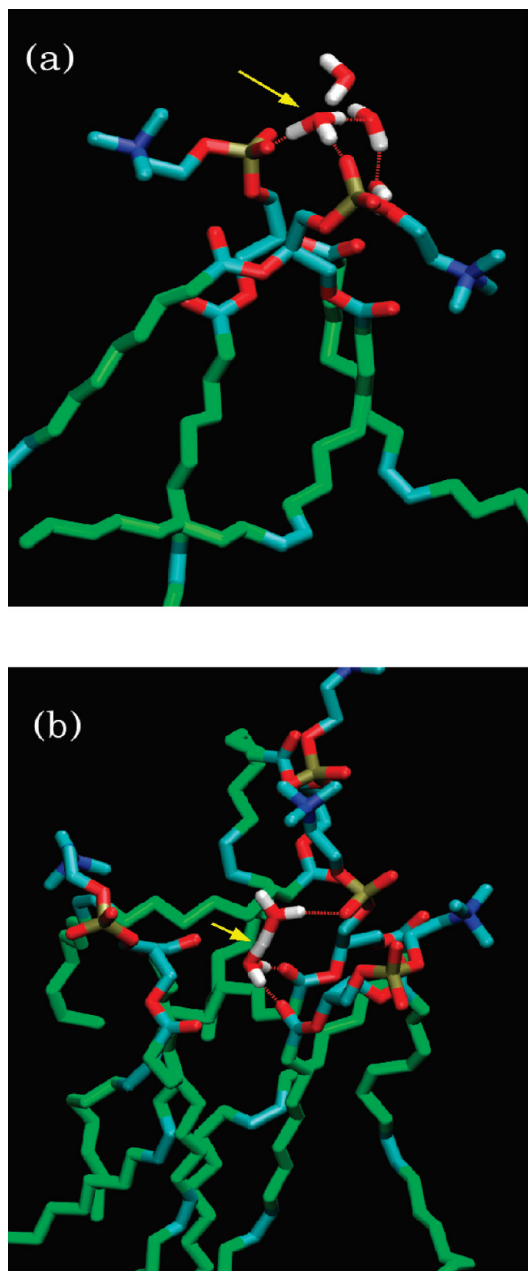


Figure 4. Typical structures of hydrated excess proton locating in (a) the shallow interface region and (b) the deep interface region of the DOPC bilayer. Yellow arrows point to the location of the hydrated excess proton.

group sites that are 6 Å apart from one another. The deep interface region is surrounded not only by the phosphate oxygen atoms but also by the carbonyl oxygen atoms, and the highest peak of the radial distribution function of the two sites is located at 6.5 Å. Therefore, the system may be stabilized by forming a bridged structure of the Zundel-like cation between these negative sites. This unique structure was first reported in ref 19.

Figure 4a shows a typical structure of the hydrated excess proton at the shallow interface ($z = 21$ Å). The corresponding charge defect is localized to the hydronium-like structure ($l_{c_0}^2 = 0.84$), which is bound to the two phosphate oxygen atoms. Figure 4b shows a Zundel-like structure ($l_{c_0}^2 = 0.59$) in the deep interface region ($z = 17$ Å), which is bound to the phosphate oxygen and carbonyl oxygen atoms. As seen in Figure 3c, the $l_{c_0}^2$ distribution is better converged by the long unbiased

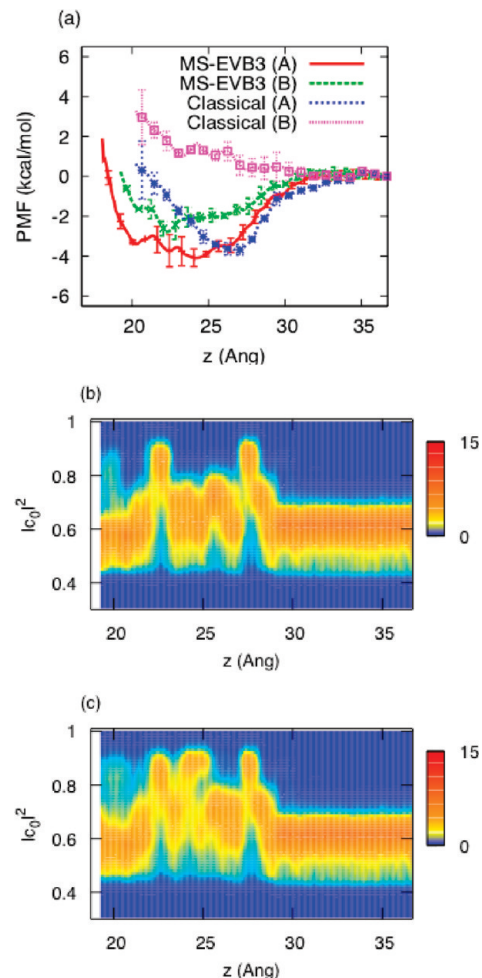


Figure 5. (a) PMF curves with respect to the z coordinate of CEC for DOPE membrane. Curve A is calculated from both biased and unbiased MD simulations, whereas curve B is calculated from the biased MD alone. (b) Distribution of the largest MS-EVB state population calculated from the biased MD alone. (c) Distribution of the largest MS-EVB state population calculated from the biased and unbiased MD.

MD data in the deep interface region ($14 < z < 18$ Å), and the Zundel-like cation probability is more enhanced. This implies that it takes nanosecond time scales to form the bridged Zundel–lipid structure, which stabilizes the excess proton considerably in this region.

4.2. DOPE Membrane. In the same way as in the DOPC simulations, PMF curves were evaluated for the DOPE bilayer. Figure 5a shows the PMF curves with respect to the z coordinate of the hydrated proton CEC for DOPE. The excess proton is again stabilized in the region of $18 \leq z \leq 26$ Å, where the anionic phosphate groups are distributed. In the DOPE membrane simulation, including the long unbiased trajectory data deepens the wells by 2 kcal/mol around $18 \leq z \leq 26$ Å, but this change is not as large as it was in the DOPC simulation. Although simulations using a more approximate hydrated proton model for the DLPE bilayer gave a high barrier in the PMF curve and the interface region had high free energy compared with the bulk water region,³⁴ the present PMF curve for the DOPE membrane shows that no high barrier exists between the bulk water region and the interface region. Moreover, the deep interface region is 4 kcal/mol lower in free energy than the bulk water region for the hydrated proton.

Figure 5b and 5c show the $l_{c_0}^2$ distributions calculated by the short biased MD and the result from combining the short

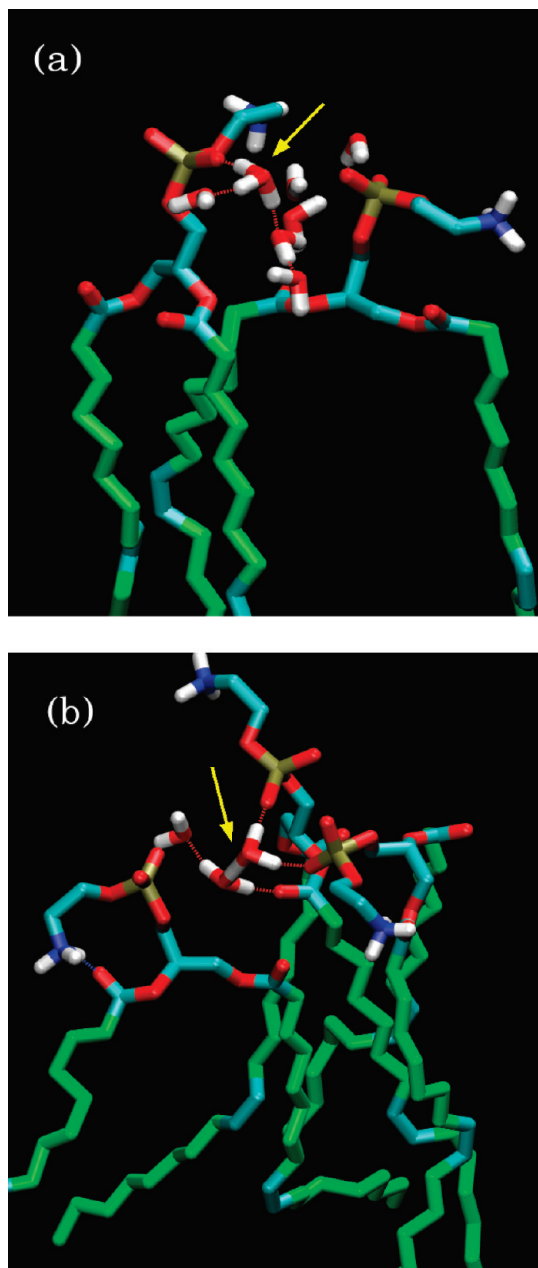


Figure 6. Typical structures of hydrated excess proton locating in (a) the shallow interface region and (b) the deep interface region of the DOPE bilayer. Yellow arrows point to the location of the hydrated excess proton.

biased and long unbiased MD simulations, respectively. A strong hydrophilic effect can be seen at $z = 27$ Å where the distribution of $lc_0|^2$ is suddenly shifted to large values. This behavior, which is the same as in the DOPC system, means that the excess charge becomes more localized to a hydronium-like structure. However, both localization and delocalization of the excess charge are seen in the free energy minimum region $18 \leq z \leq 26$ Å, where $lc_0|^2 + lc_1|^2 \geq 0.9$. This suggests that the excess proton changes its localization propensity depending on the surrounding negative lipid site distribution.

Figure 6a and 6b show structures of the hydrated excess proton located at the shallow interface ($z = 27$ Å) and the deep interface ($z = 23$ Å), respectively. While the charge defect is fairly localized in Figure 6a ($lc_0|^2 = 0.69$), it is more delocalized in Figure 6b ($lc_0|^2 = 0.53$). Figure 6b also shows that the two phosphate oxygen atoms and the carbonyl oxygen atom

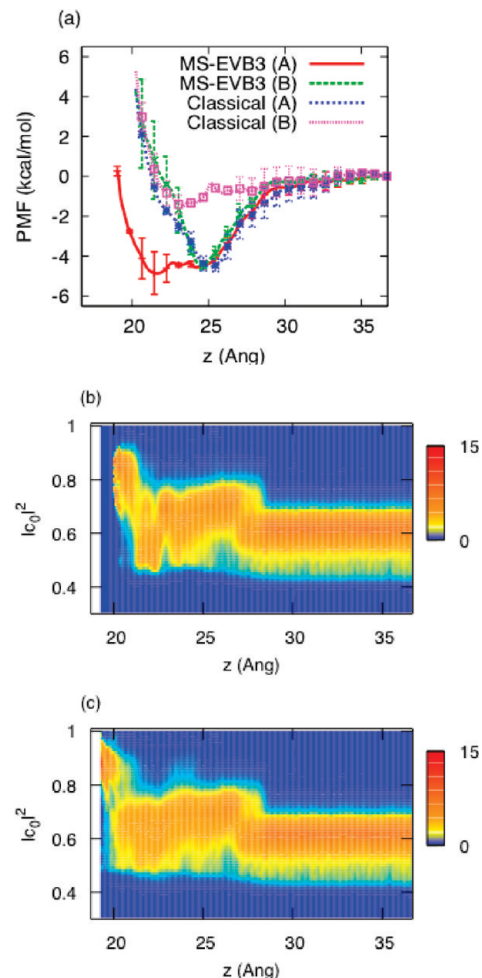


Figure 7. (a) PMF curves with respect to the z coordinate of CEC for DOPG membrane. Curve A is calculated from both biased and unbiased MD simulations, whereas curve B is calculated from the biased MD alone. (b) Distribution of the largest MS-EVB state population calculated from the biased MD alone. (c) Distribution of the largest MS-EVB state population calculated from the biased and unbiased MD.

coordinate and stabilize the distorted Zundel-like cation. In Figure 5c, it can be seen that the long unbiased MD simulation data also affect the $lc_0|^2$ distribution in the deep interface region, though the effect is smaller than in the DOPC system.

4.3. DOPG Membrane. Figure 7a shows the PMF curves for the DOPG membrane system. Without including the data from the long unbiased trajectory, the global minimum is located at $z = 25$ Å with a 5 kcal/mol depth. This region corresponds to the shallow interface region (see Figure 2). As shown in Figures 7b and 7c, the distribution of $lc_0|^2$ becomes wider ($0.45 \leq lc_0|^2 \leq 0.75$) around this region. Similar to the DOPC and the DOPE systems, there is also not a high barrier for adsorbing the excess proton.

Although there are no major differences between Figure 7b and 7c, the PMF minimum in Figure 7a becomes significantly deeper at $z \leq 24$ Å when the data from the long unbiased trajectory are included. The additional 2 ns unbiased MD sampling was performed because the standard deviation of the PMF calculated from the umbrella sampling and the 5 ns MD sampling was still relatively large. This large deviation is probably due to the slow lipid motion. For example, Zhao et al.³⁵ suggested that the forming and breaking of the Na^+ –lipid bonds are slow processes similar to the lateral diffusion of the lipid. The region at $z = 22$ Å is still near the center of the

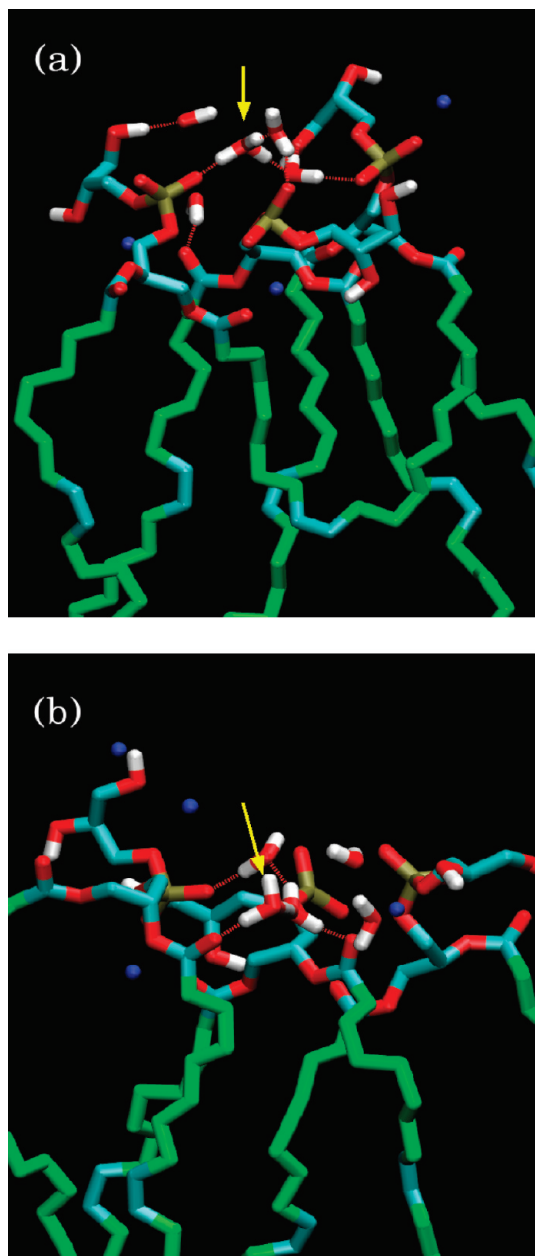


Figure 8. Typical structures of hydrated excess proton locating in (a) the shallow interface region and (b) the deep interface region of the DOPG bilayer. Yellow arrows point to the location of the hydrated excess proton.

phosphorus distribution, but the excess charge is delocalized as seen in Figure 4c, where $|c_0|^2 + |c_1|^2 \geq 0.9$. This suggests the formation of the distorted Zundel-like ion bridge is again important as seen in the DOPC system.

The typical hydrated proton structures are given in Figure 8. The structure in Figure 8a corresponds to the global minimum ($z = 25$ Å) of the PMF calculated from the short umbrella sampling data (the green curve in Figure 7a). The hydrated proton is coordinated by one phosphate oxygen atom, and the charge defect is localized to a hydronium-like structure ($|c_0|^2 = 0.69$). Figure 8b shows a structure of the hydrated proton located near the minimum of the PMF calculated from the longer unbiased trajectory as well as the umbrella sampling data ($z = 22$ Å). Though the value of $|c_0|^2$ is 0.63, the charge defect is highly localized to one H_5O_2^+ structure. As discussed for DOPC and DOPE, it can be seen that this Zundel-like cation bridges the lipid anionic atoms.

5. Effect of Charge Defect Delocalization: Comparison with the Classical Hydronium Model

To further clarify the effect of the charge defect delocalization associated with the excess proton, the classical hydronium cation model was also simulated. The simulation conditions were the same as in the MS-EVB3 simulation. A 400 ps MD simulation was carried out in each of the umbrella window regions, and a 5 ns unbiased MD simulation was also carried out as for the MS-EVB3 model. The sampled data were combined using the WHAM^{49,50} algorithm to estimate the respective PMF curves. For the three membranes, the long unbiased trajectories improved the PMF curves as shown in Figures 3a, 5a, and 7a and deepened the global minima in the shallow interface regions.

For the DOPC membrane in Figure 3a, a small barrier at $z = 24$ Å disappeared and the global minimum at $z = 22$ Å became 3 kcal/mol deeper with the inclusion of the nanosecond order MD sampling. The PMF of the classical model is very similar to that in the MS-EVB3 model in the shallow interface region ($z \geq 20$ Å). However, the PMF of the classical hydronium model is destabilized compared to that of the MS-EVB3 model in the deep interface region. This discrepancy is due to the charge defect delocalization present in the MS-EVB3 model and presumably in reality. In fact, the MS-EVB3 simulation shows that the Zundel-like cation structure is favorable in the deep interface region. By contrast, the classical hydronium has a localized positive charge, so the classical hydronium is therefore unstable in this region. Note that the Na^+ cation, whose charge cannot be delocalized, is also stabilized in the shallow DMPC interface region but not beyond.²¹

The PMF calculated by the 400 ps biased MD simulations (Figure 5a) suggests that the classical hydronium prefers the bulk water region rather than the shallow interface region for the DOPE membrane. However, including the long MD simulation data creates a 4 kcal/mol well at $z = 27$ Å. As seen in the DOPC system, the better converged PMF of the classical hydronium model is consistent with that of MS-EVB3 model in the shallow interface region. It is also seen for the DOPE system that the classical hydronium cannot enter the deeper interface regions, due to the missing charge defect delocalization physics of the classical model.

For the DOPG membrane (Figure 7a), although the PMF curve of the short biased MD has a very shallow minimum, including the data from the long MD sampling again lowers the free energy in the shallow interface region. The depth of global minimum is 5 kcal/mol, and the better converged PMF curve is similar to the PMF of the MS-EVB3 model in the shallow interface region. In the deep interface region, the classical hydronium is again unstable, similar to the behavior for the DOPC and DOPE interfaces, due to its inability to capture the correct behavior of the delocalization of the excess proton charge defect. Therefore, it can again be concluded that an appropriate description of the charge defect delocalization is crucial to the study of the hydrated excess proton behavior near the lipid membrane.

It is also instructive to compare the DOPE system simulated here to the DLPE system investigated by Zahn and Brickmann.³⁴ The excess proton prefers the bulk water region in the latter simulations reported for the DLPE system, and the PMF curve has a high barrier at the entrance of the interface region. (The PMF values measured from the bulk water region are 10 and 20 kcal/mol at the local minimum of the interface and the transition state, respectively.) This simulation result would seem to indicate that the DLPE membrane does not act as a proton-collecting antenna even though these two lipids have the same

TABLE 1: Diffusion Coefficients ($\text{\AA}^2/\text{ps}$) for the Hydrated Excess Proton CEC, Classical Hydronium Cation, and Lipid Head Group Phosphorus

system	CEC (MS-EVB3)	classical hydronium	phosphorus
DOPC interface	0.015 ± 0.003	0.017 ± 0.003	0.0113 ± 0.0006
DOPE interface	0.022 ± 0.005	0.030 ± 0.006	0.0121 ± 0.0006
DOPG interface	0.041 ± 0.003	0.025 ± 0.002	0.0126 ± 0.0003
bulk water (308 K)	0.346 ± 0.025	0.121 ± 0.004	—

PE head group. The present results, based on a different simulation model and methodology, suggest that the DOPE membrane has a pronounced proton-collecting effect, similar to the DOPG and the DOPC systems. Such large differences seem unreasonable, even though the area/lipid of DLPE (46.8 \AA^2) is slightly smaller than that of DOPE (51.9 \AA^2). Interestingly, the PMF of DLPE from ref 34 is very similar to the classical PMF of DOPE calculated from the 400 ps biased MD simulations. This result implies that both the model and convergence of the DLPE simulations are in error. For example, the excess proton force field of the DLPE simulation³⁴ was essentially based on the two-state EVB model.⁵² Although this model can describe the excess proton charge defect delocalization to some extent, the charge distribution in this model is much more limited than in the MS-EVB3 model, and thereby the former model can be considered to be closer to the classical hydronium model. Also, a 50 ps trajectory was used for each window of the umbrella sampling in ref 34 for the DLPE system. As discussed earlier, this is much too short to describe the reorientation of the lipids and to obtain a reasonably well-converged PMF result.

6. Dynamic Behavior of the Hydrated Excess Proton

To characterize the dynamics of the hydrated excess proton near the lipid membrane surface, the lateral diffusion coefficients were estimated from the unbiased MD simulations. While the last 3 ns of trajectory was used for the DOPE system, the last 4 ns of trajectories were used for the DOPC and DOPG systems in order to calculate the lateral mean square displacements near the lipid membranes. Each lateral mean square displacement as a function of time was fit to a linear line in the region of $1 \leq t \leq 10$ ps. From the gradient of the linear line, the lateral diffusion coefficient was obtained. The resultant coefficients are 0.015, 0.022, and $0.045 \text{ \AA}^2/\text{ps}$ for the DOPC, DOPE, and DOPG systems, respectively, as shown in Table 1. These values agree reasonably well with the value ($0.023 \text{ \AA}^2/\text{ps}$) calculated for the DMPC membrane with the MS-EVB2 model,¹⁹ and are 1 order of magnitude smaller than the value of the diffusion coefficient for the protonated bulk water systems. Thus, the diffusion coefficient of the excess proton in 216 water molecules is $0.286 \text{ \AA}^2/\text{ps}$ at $T = 298.15 \text{ K}$ and $0.346 \text{ \AA}^2/\text{ps}$ at $T = 308 \text{ K}$, both with constant NVT dynamics using the Nose–Hoover thermostat ($\tau_T = 0.2 \text{ ps}$). Note that the value of $0.286 \text{ \AA}^2/\text{ps}$ at 298.15 K agrees well with the value ($0.29 \text{ \AA}^2/\text{ps}$) previously calculated by the constant NVE MS-EVB3 MD simulations.³¹ These lateral diffusion coefficients for the excess proton agree with the diffusion coefficients of the phosphorus atoms of the lipid head groups (see Table 1). This implies that the excess proton moves in conjunction with the lipid head groups.

Note that the lateral diffusion coefficients of phosphorus atoms calculated here are 1 order higher than those of the previous simulations^{53,54} and experiments.^{55,56} This is because the time scale studied in this work is too short to describe the two-dimensional fluidity of the lipid bilayer, and therefore

the calculated diffusion coefficients correspond to the local fluctuations of the lipid head groups. However, the experimental value of the lipid diffusion coefficient is similar to that of the proton diffusion coefficient near the bilayer; Brändén et al.²⁸ estimated the diffusion coefficient of proton on the DOPG liposome to be $0.002 \text{ \AA}^2/\text{ps}$ from fluorescence correlation spectroscopy measurements, whereas the experimental value of the lipid diffusion coefficient is $0.0002\text{--}0.003 \text{ \AA}^2/\text{ps}$.⁵⁶ This experimental result also implies that the hydrated excess proton is almost always trapped on the lipids and moves in conjunction with the lipids even on the experimental (microsecond) time scale.

However, this slow proton diffusion is inconsistent with some experimental results that suggest the excess proton diffusion along the membrane is not so slow. For example, Serowy et al.²⁷ reported the proton diffusion coefficient to be $0.58 \text{ \AA}^2/\text{ps}$, which is almost half of the diffusion coefficient of the proton in bulk water. They used DPhPC, whose tail group is different from that of DOPC but the head group is the same as that of DOPC. Therefore, the proton behavior on DPhPC interface might be quite similar to that on the DOPC interface. As shown in Table S1 in the Supporting Information, fast diffusion of the proton can occur only in the very shallow interface region. The MD simulation in this work shows that the proton remains in the shallow interface region during the first 100 ps. Smondyrev and Voth¹⁹ also reported a similar fast motion of a 160 ps trajectory at the shallow interface region. Such a metastable state might be realized by the roughness of the lipid membrane surface (see Figure S1b in the Supporting Information). Therefore, it can be considered that the fast diffusion measured in the experiment occurs in the shallow interface region. However, this explanation still conflicts with the possibility that the excess proton runs along the membrane surface over several nanoseconds in experiments.

While the membrane collects protons from bulk water (pH 8–10) in the experiment of Brändén et al.,²⁸ many protons are produced at the source region in the experiment of Serowy et al.²⁷ In short, these experiments were carried out under different pH conditions. From this viewpoint, it is possible that some protons are trapped at negative sites of the membrane and prevent other protons from approaching these sites in the low pH experiment of Serowy et al. Then, it is possible that Serowy et al. might have measured the diffusion of such mobile protons, but not the trapped protons. In the future, it will be important to investigate the pH dependence of proton diffusion to understand the proton translocation process along real biological membranes.

It is also found that the proton trapped on the membrane interface shows subnanosecond dynamics. Figure 9 shows the distributions of the largest EVB state population, $|c_0|^2$, sampled for 200 ps windows. All the $|c_0|^2$ distributions on the membrane surface are different from that in pure water due to strong electrostatic interaction. On the DOPC membrane, the center of excess charge is delocalized from 2.0 to 2.2 ns, but gradually becomes localized from 2.4 to 2.6 ns. The excess charge starts to be delocalized again from 2.8 to 3.0 ns. For the DOPE system, similar behavior can be seen in Figure 9b. Although the variation for the DOPG membrane shown in Figure 9c is smaller than those for DOPC and DOPE, the $|c_0|^2$ distribution changes in the subnanosecond time scale. These slow motions are probably related to the fact that the nanosecond order MD sampling is required to evaluate the PMF curve.

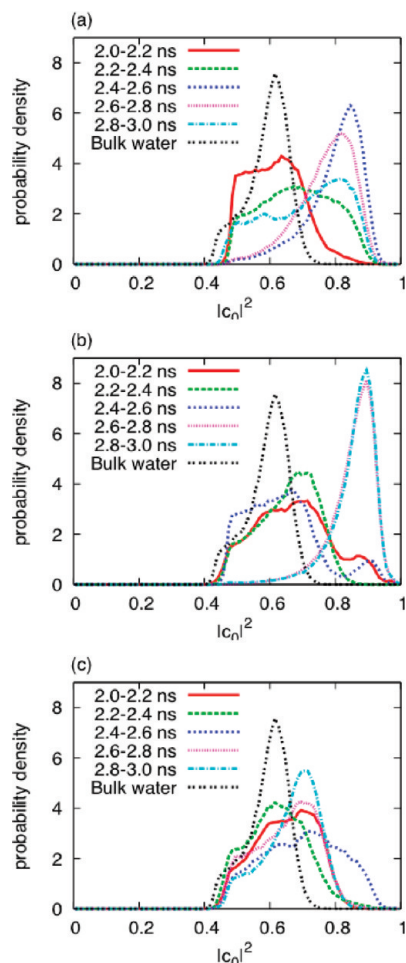


Figure 9. Distributions of the largest MS-EVB state population, $|c_n|^2$, during 200 ps in (a) the DOPC system, (b) the DOPE system, and (c) the DOPG system.

7. Effect of Phosphate Protonation

In the MS-EVB MD simulation reported earlier, the phosphate protonation was never included directly, because of the low pK_a (~ 2) of the phosphate, which is likely due to the fact that the pK_a value for the first proton dissociation of phosphoric acid is 2. Since the depths of the hydrated excess proton PMF curves are at most 6 kcal/mol as shown in Figures 3a, 5a, and 7a, the pH at the interface is about 3 under the assumption that the bulk water region is pH 7. However, the estimated pK_a value of the phosphate may not be low enough. Also, the lipid membrane interface might be different from that of bulk water, because the water molecules are confined by the lipid head groups to remain in the interface region.

To investigate the possibility of the lipids being protonated, 600 ps trajectories were calculated for the DOPC, DOPE, and DOPG membrane systems with a protonatable lipid force field, which was developed in the MS-EVB framework based on ab initio calculations. Detailed information on this force field is given in the Appendix. The equilibrated configuration of the unprotonatable lipid simulation was used as the initial configuration for each lipid membrane system.

In the 600 ps MD simulations, the protonatable sites of the lipids solvated the hydrated excess proton, but the lipids were never protonated for any of the three membranes. This result suggests that the lipid prefers the unprotonated state and the excess proton is trapped as a contact ion pair, which causes the high proton concentration in the interface region. This result is

also consistent with that of dimethyl phosphate (DMP). In fact, it is found that the contact ion pair well in the PMF curve of DMP system (see the Appendix). From the analogy with DMP, it can be expected that the proton should quickly dissociate from DMP even if the lipid is protonated. In light of these results, the unprotonatable lipid model is likely a good approximation.

8. Concluding Remarks

In this work, the statistical and dynamic behavior of the excess proton was systematically studied near DOPC, DOPE, and DOPG membranes. It was found that nanosecond order sampling and an appropriate description of proton shuttling are required to calculate the PMF curves. All the global minima of the PMF curves are deeper than 4 kcal/mol. These results suggest that the lipid membranes have a stronger proton-collecting antenna effect than previously estimated. The result of the strong antenna effect is consistent with the recent experiment of Brändén et al.²⁸

Through the analysis of the solvation structure of excess proton, it is found that the distorted Zundel-like cation is extensively formed in the deep interface region for all the DOPC, DOPE and DOPG systems. The Zundel-like cation bridges the negative sites of the phosphate groups and the carbonyl groups, which stabilize the hydrated excess proton in this region. This result may also be related to the recent experiment of the proton transfer in the gramicidin (gA) channels⁵⁷ that have shown the proton conductance rates in the gA channels are highly enhanced by the phosphate group of the membranes, compared to gA channels in the membranes made of monoglycerides or ceramides. The latter membrane molecules have the almost same structures as the phospholipids, but they have a phosphocholine as a hydrophilic head group. It was found that the proton conductance in the gA channels was significantly higher in the phospholipid membrane, presumably due to the presence of the phosphate groups. According to previous MS-EVB MD simulation results,⁵⁸ one important effect of the phosphate group is ordering water molecules at the bilayer interface, which decreases the free energy barrier for the hydrated excess proton around the entry/exit region of the gA channel. Another significant possible effect of the phosphate group is the proton-collecting antenna effect. As proposed by Brändén et al.,²⁸ the phospholipid membrane collects hydrated excess protons and provides them to the proton channels efficiently. As shown in this paper, the proton-collecting antenna effect arises because the phosphate groups stabilize the hydrated proton along with the carbonyl groups. In this vein, the difference between Figures 3a and 5a shows that the proton-collecting effect of the DOPC membrane is stronger than that of the DOPE membrane, which is consistent with the experimental result that the proton conductance in the gA channel is higher in the POPC membrane than in the POPE membrane.⁵⁹

To characterize the dynamic behavior of the proton transport, the lateral diffusion coefficients were calculated. Once the hydrated excess proton is trapped near the lipid, the excess proton follows the lipid motion, and the lateral diffusion becomes significantly slower than in bulk water. At a high proton concentration, it can be expected that some protons will be trapped on the membrane, preventing other protons from subsequently being strongly bound by the membrane. Such weakly bound protons can diffuse faster than strongly bound protons, which may be measured in low pH experiments.

Finally, the effect of the phosphate protonation was investigated. The phosphate group protonation was never observed in

TABLE 2: On-Site Charges of Dimethyl Phosphate and Hydrogen Dimethyl Phosphate

	DMP ⁻ + H ⁺	DMPH	transferred charge
P	+1.02	+1.05	+0.03
CH ₃	+0.23	+0.28	+0.05
O(ester)	-0.47	-0.41	+0.06
O(ionic)	-0.77	-0.65	+0.12
O(reactive)	-0.77	-0.65	+0.12
H	+1.00	+0.51	-0.49

the 600 ps MD simulations for the DOPC, DOPE, and DOPG membranes. This behavior is consistent with the fact the PMF for the DMP protonation has a considerably deep well corresponding to the contact ion pair compared with the DMPH well. Furthermore, the protonation is slower than the deprotonation, because the free energy barrier of the protonation is much higher than that of the deprotonation. This means that the excess proton dissociates quickly from DMP even if the DMP is protonated. From these results, the lipid head group protonation effect is believed to be so small that the unprotonatable lipid force field is a good approximation, thus justifying the present unprotonated lipid MS-EVB simulations.

Acknowledgment. This research was supported in part by the National Science Foundation (CHE-0719522). We thank Drs. C. M. Maupin, L. Lu, R. Hills, and C. Knox for their valuable discussions and assistance. T.Y. acknowledges the Promotion of Science for Young Scientists of Japan for support of this study. The computational resources have been provided in part by the National Science Foundation via the TeraGrid. The molecular images in this article were created with the molecular graphics program VMD.⁶⁰

Appendix: MS-EVB Model for the Interaction between an Excess Hydrated Proton and a Dimethyl Phosphate

To investigate the interaction between the negative phosphate group and the hydrated excess proton, dimethyl phosphate (DMP) was introduced as a simplest model molecule of a phosphodiester, which is a common part of all the phospholipid molecules.

Correlation between an Excess Proton and a Classical Dimethyl Phosphate. First, the interaction between a hydrated excess proton and a classical DMP anion was investigated. The force field parameters of DMP were the same as those of the lipid phosphate part, except for the site charges tabulated in Table 2. These site charges were derived from B3LYP/6-31+G(d)/CPCM⁶¹ ab initio calculations with the charges from electrostatic potentials obtained using a grid based method (CHELPG).⁶² Note that all the ab initio calculations were carried out with the Gaussian 03 program package.⁶³ The Nose–Hoover constant NVT MD simulations⁴¹ with umbrella potentials were performed in a $24.61 \times 24.61 \times 24.61$ Å cubic box at $T = 298.15$ K to calculate the PMF curve for the excess proton CEC. The system consisted of the DMP and the excess proton solvated in 500 water molecules.

Figure 10a shows the PMF curve as a function of the distance, r , between the phosphorus and the CEC for both the MS-EVB3 system and the classical hydronium system. The global minima of the PMF curves correspond to the contact ion pair of the hydronium and anionic oxygen atom, and the minimum of the classical hydronium model is as deep as that of the MS-EVB3 model. However, the PMF curve of the classical model has a narrower global minimum well and another shallow well corresponding to the case that the hydronium

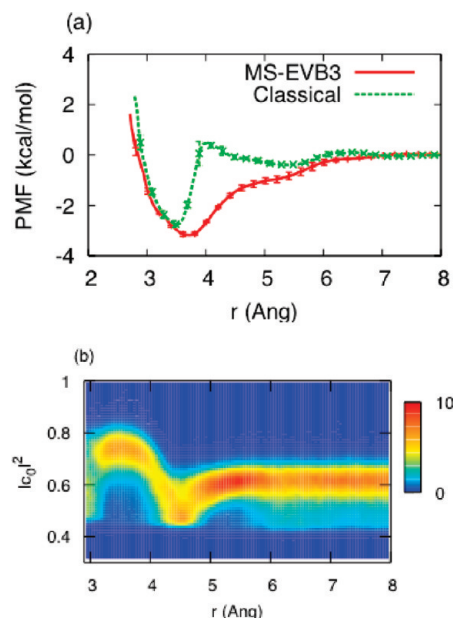


Figure 10. (a) PMF curves with respect to the distance (r) between phosphorus and CEC for the DMP system. Red and green lines are calculated with the MS-EVB model and classical hydronium model, respectively. (b) Distribution of the largest MS-EVB state population as a function of r .

is in the second solvation shell, while the PMF curve of the MS-EVB3 model has only one large minimum. Thus, the classical hydronium feels a barrier when transferring from the second solvation shell to the first solvation shell. On the other hand, the shuttling excess proton described by the MS-EVB3 model does not feel a repulsive force on average when approaching the phosphate.

The distribution of the largest EVB state population, $|c_0|^2$, is shown in Figure 10b as a function of the distance, r , between phosphorus and the CEC. In the region of $r \geq 5.5$ Å, the distribution is almost the same as that in bulk water. However, when the excess proton approaches the phosphate, the largest EVB state population, $|c_0|^2$, is decreased gradually and distributed around 0.5 in the vicinity of $r = 4.5$ Å. This region lies between the first and second solvation shells of the anionic oxygen of the DMP. Therefore, the enhancement of the Zundel cation stabilizes the PMF in the region between the first and second solvation shells and removes the barrier seen in the classical PMF curve. Then the excess charge is localized with increasing the electrostatic stabilization in the first solvation shell ($r = 3.5$ Å).

From the dynamic viewpoint, the formation of Zundel cation between the first and second solvation shells means that the proton shuttling (Grotthuss) mechanism is important for the excess proton to solvate the anionic oxygen site directly. In contrast, the classical hydronium cannot shuttle an excess proton to a neighbor water molecule, and therefore the hydronium in the second solvation shell has to be exchanged for a water molecule in the first solvation shell. This exchange motion is slower than the proton shuttling. It is likely that the same slow motion happens for the classical hydronium near the lipid membranes.

Protonatable MS-EVB Model of Dimethyl Phosphate. To study the protonation of phosphate group, the proton transfer between the hydronium and DMP was treated within the MS-EVB model, as in the case of amino acids.⁶⁴ In the classical part of the model, \mathbf{H}_0 , the OH bond potential of the hydrogen

TABLE 3: MS-EVB Parameters for the DMP

parameter	value
V_{ii}^0	−96.513 kcal/mol
V_{ij}^{const}	−15.262 kcal/mol
r_{sc}^0	1.135 Å
λ	0.047
R_{DA}^0	2.500 Å
C	0.531
α	1.366 Å ^{−2}
a_{DA}	3.610 Å
β	1.628 Å ^{−2}
b_{DA}	3.163 Å
ε	1.228 Å ^{−1}
c_{DA}	3.234 Å
γ	0.224 Å ^{−2}

dimethyl phosphate (DMPH) is given by the standard Morse potential

$$U_{\text{M}}(r_{\text{OH}}) = D_0(1 - \exp(-a(r_{\text{OH}} - r_0)))^2 \quad (5)$$

where $D_0 = 76.8$ kcal/mol, $a = 2.37$ Å^{−1}, and $r_0 = 0.99$ Å. The center of the harmonic angle potential HOP is taken to be 116.0°. These parameters were determined based on B3LYP/6-31+G(d)/CPCM,⁶¹ whereas the other classical parameters were taken from GROMOS96.³⁸ This classical part of the model also involves a constant term, V_{ii}^0 , which adjusts the energy difference between the DMPH EVB state and the H₃O⁺ EVB state.

The off-diagonal term of \mathbf{V} is given by

$$V_{ij} = V_{ij}^{\text{const}} f(R_{\text{DA}}) g(q) \quad (6)$$

where R_{DA} is the distance between the donor site D and the acceptor site A, and q is the proton-transfer coordinate defined as

$$q = \left| R_{\text{DH}^+} - r_{\text{sc}} \frac{R_{\text{DA}}}{2} \right| \quad (7)$$

Here, R_{DH^+} is the distance between the donor site D and excess proton and $r_{\text{sc}} = r_{\text{sc}}^0 - \lambda(R_{\text{DA}} - R_{\text{DA}}^0)$. The functions f and g are given by

$$f(R_{\text{DA}}) = \{C \exp(-\alpha(R_{\text{DA}} - a_{\text{DA}})^2) + (1 - C) \exp(-\beta(R_{\text{DA}} - b_{\text{DA}})^2)\} \{1 + \tanh(\varepsilon(R_{\text{DA}} - c_{\text{DA}}))\} \quad (8)$$

$$g(q) = \exp(-\gamma q^2) \quad (9)$$

where the parameters were fit to the B3LYP/6-31G+(d)/CPCM⁶¹ energies of the DMPH(H₂O)₃ cluster and the fitting error was 0.8 kcal/mol. These MS-EVB parameters are tabulated in Table 3. Note that the diagonal element of \mathbf{V} (the repulsion term) is not included in this case.

Figure 11a shows the PMF curve as a function of distance between the phosphorus and excess proton CEC. The simulation conditions were the same as above. To check the accuracy of this model, the pK_{a} was estimated from the PMF curve. The resultant pK_{a} value is -1.54 ± 0.09 , which is somewhat lower than the experimental value of 0.76.⁶⁵ Compared with the nonprotonatable model, the PMF curve is quite similar in the

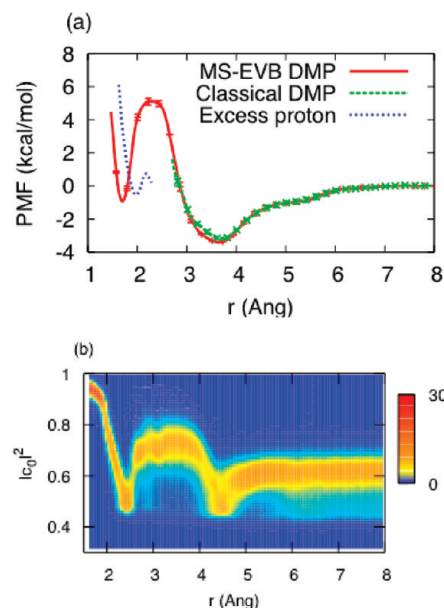


Figure 11. (a) PMF curves with respect to the distance (r) between phosphorus and CEC for DMP system. Red and green lines are calculated with the MS-EVB DMP model and classical DMP model, respectively. The blue line is the PMF curve as a function of the distance between the excess proton and DMP. Once the hydronium is formed after deprotonation, the “excess proton” can no longer be identified, and the PMF curve cannot be defined straightforwardly. (b) Distribution of the largest MS-EVB state population as a function of r .

region of $r \geq 3$ Å. This means that the classical DMP model is a good approximation unless the protonation becomes important under the low pH condition. The essential difference is found only in the region of $r \leq 3$ Å. In this region, the transition state can be seen at $r = 2.5$ Å and the local minimum corresponding to the protonated state (DMPH) is located at $r = 1.8$ Å. The contact ion pair well ($r \approx 4$ Å) is much more stabilized than the protonated DMPH well. This implies that the contact ion pair is rather dominant statistically. Near the transition state, the excess proton is shared by the DMP and the water molecule, and then the excess charge is delocalized, as shown in Figure 11b, whereas the excess charge is extensively localized to the DMPH at the local minimum ($r = 1.8$ Å).

To consider the protonation/deprotonation rate from the free energy barrier, one must transform the CEC coordinate to the excess proton coordinate, because the CEC position is changed mainly by the charge transfer (the change of the c_i) around the transition state. In other regions, the CEC motion is dominated by the excess proton motion. Thus, the population density around the transition state looks lower in the CEC coordinate than in the excess proton coordinate, and thereby the free energy barrier looks higher in the CEC coordinate. The PMF curve as a function of the excess proton coordinate is shown by the blue line in Figure 11a. The barrier height for the deprotonation is 1.4 kcal/mol, which means the proton dissociates from the DMP reasonably quickly even if the DMP is protonated. Once the hydronium is formed after the deprotonation, a single “excess proton” is no longer well-defined, because the three hydrogen nuclei of the hydronium are equivalent. Thus, it is difficult to estimate the protonation barrier height. However, since the free energy difference between the DMPH state and the contact ion pair state is 2.4 kcal/mol, as shown by the red curve, it can be considered that the protonation barrier height is about 4 kcal/mol and therefore the protonation is much slower than the deprotonation. Note that a value of $V_{ii}^0 = -43.961$ kcal/mol is

adopted for the protonatable lipid force field. This value was determined from the same ab initio data. The fitting error was smaller than 1 kcal/mol.

Supporting Information Available: Figure S1 showing additional electrostatic potentials generated by the lipids and Table S1 giving a detailed listing of the diffusion coefficients. This material is available free of charge via the Internet at <http://pubs.acs.org>.

References and Notes

- (1) Petersen, M. K.; Iyengar, S. S.; Day, T. J. F.; Voth, G. A. *J. Phys. Chem. B* **2004**, *108*, 14804–14806.
- (2) Mucha, M.; Frigato, T.; Levering, L. M.; Allen, H. C.; Tobias, D. J.; Dang, L. X.; Jungwirth, P. *J. Phys. Chem. B* **2005**, *109*, 7617–7623.
- (3) Petersen, P. B.; Saykally, R. J. *J. Phys. Chem. B* **2005**, *109*, 7976–7980.
- (4) Burnham, C. J.; Petersen, M. K.; Day, T. J. F.; Iyengar, S. S.; Voth, G. A. *J. Chem. Phys.* **2006**, *124*, 024327.
- (5) Gopalakrishnan, S.; Liu, D. F.; Allen, H. C.; Kuo, M.; Shultz, M. J. *Chem. Rev.* **2006**, *106*, 1155–1175.
- (6) Morrone, J. A.; Haslinger, K. E.; Tuckerman, M. E. *J. Phys. Chem. B* **2006**, *110*, 3712–3720.
- (7) Pegram, L. M.; Record, M. T. *Proc. Natl. Acad. Sci. U.S.A.* **2006**, *103*, 14278–14281.
- (8) Petersen, M. K.; Voth, G. A. *J. Phys. Chem. B* **2006**, *110*, 18594–18600.
- (9) Tarbuck, T. L.; Ota, S. T.; Richmond, G. L. *J. Am. Chem. Soc.* **2006**, *128*, 14519–14527.
- (10) Buch, V.; Milet, A.; Vacha, R.; Jungwirth, P.; Devlin, J. P. *Proc. Natl. Acad. Sci. U.S.A.* **2007**, *104*, 7342–7347.
- (11) Ishiyama, T.; Morita, A. *J. Phys. Chem. A* **2007**, *111*, 9277–9285.
- (12) Levering, L. M.; Sierra-Hernandez, M. R.; Allen, H. C. *J. Phys. Chem. C* **2007**, *111*, 8814–8826.
- (13) Vacha, R.; Buch, V.; Milet, A.; Devlin, P.; Jungwirth, P. *Phys. Chem. Chem. Phys.* **2007**, *9*, 4736–4747.
- (14) Wick, C. D.; Kuo, I. F. W.; Mundy, C. J.; Dang, L. X. *J. Chem. Theory Comput.* **2007**, *3*, 2002–2010.
- (15) Jungwirth, P.; Winter, B. *Annu. Rev. Phys. Chem.* **2008**, *59*, 343–366.
- (16) Selvan, M. E.; Liu, J.; Keffer, D. J.; Cui, S.; Edwards, B. J.; Steele, W. V. *J. Phys. Chem. C* **2008**, *112*, 1975–1984.
- (17) Wang, F.; Izvekov, S.; Voth, G. A. *J. Am. Chem. Soc.* **2008**, *130*, 3120–3126.
- (18) Iuchi, S.; Chen, H. N.; Paesani, F.; Voth, G. A. *J. Phys. Chem. B* **2009**, *113*, 4017–4030.
- (19) Smondyrev, A. M.; Voth, G. A. *Biophys. J.* **2002**, *82*, 1460–1468.
- (20) Tepper, H. L.; Voth, G. A. *Biophys. J.* **2005**, *88*, 3095–3108.
- (21) Tepper, H. L.; Voth, G. A. *J. Phys. Chem. B* **2006**, *110*, 21327–21337.
- (22) Mulikidjanian, A. Y.; Heberle, J.; Cherepanov, D. A. *Biochim. Biophys. Acta: Bioenerg.* **2006**, *1757*, 913–930.
- (23) Gutman, M.; Nachliel, E. *Biochim. Biophys. Acta* **1995**, *1231*, 123–138.
- (24) Milhaud, J. *Biochim. Biophys. Acta: Biomembr.* **2004**, *1663*, 19–51.
- (25) Heberle, J.; Riesle, J.; Thiedemann, G.; Oesterheld, D.; Dencher, N. A. *Nature (London)* **1994**, *370*, 379–382.
- (26) Alexiev, U.; Mollaaghababa, R.; Scherrer, P.; Khorana, H. G.; Heyn, M. P. *Proc. Natl. Acad. Sci. U.S.A.* **1995**, *92*, 372–376.
- (27) Serowy, S.; Saparov, S. M.; Antonenko, Y. N.; Kozlovsky, W.; Hagen, V.; Pohl, P. *Biophys. J.* **2003**, *84*, 1031–1037.
- (28) Brändén, M.; Sandén, T.; Brzezinski, P.; Widengren, J. *Proc. Natl. Acad. Sci. U.S.A.* **2006**, *103*, 19766–19770.
- (29) Schmitt, U. W.; Voth, G. A. *J. Chem. Phys.* **1999**, *111*, 9361–9381.
- (30) Day, T. J. F.; Soudackov, A. V.; Cuma, M.; Schmitt, U. W.; Voth, G. A. *J. Chem. Phys.* **2002**, *117*, 5839–5849.
- (31) Wu, Y. J.; Chen, H. N.; Wang, F.; Paesani, F.; Voth, G. A. *J. Phys. Chem. B* **2008**, *112*, 467–482.
- (32) Voth, G. A. *Acc. Chem. Res.* **2006**, *39*, 143–150.
- (33) Swanson, J. M. J.; Maupin, C. M.; Chen, H. N.; Petersen, M. K.; Xu, J. C.; Wu, Y. J.; Voth, G. A. *J. Phys. Chem. B* **2007**, *111*, 4300–4314.
- (34) Zahn, D.; Brickmann, J. *Phys. Chem. Chem. Phys.* **2001**, *3*, 848–852.
- (35) Zhao, W.; Rog, T.; Gurtovenko, A. A.; Vattulainen, I.; Karttunen, M. *Biophys. J.* **2007**, *92*, 1114–1124.
- (36) Wu, Y. J.; Tepper, H. L.; Voth, G. A. *J. Chem. Phys.* **2006**, *124*, 024503.
- (37) Berger, O.; Edholm, O.; Jähnig, F. *Biophys. J.* **1997**, *72*, 2002–2013.
- (38) van Gunsteren, W. F.; Billeter, S. R.; Eising, A. A.; Hünenberger, P. H.; Krüger, P.; Mark, A. E.; Scott, W. R. P.; Tironi, I. G. *Biomolecular Simulation: The GROMOS96 Manual and User Guide*; BIOMOS, Groningen and vdf Hochschulverlag AG an der ETH Zürich, Zürich, 1996.
- (39) de Vries, A. H.; Mark, A. E.; Marrink, S. J. *J. Phys. Chem. B* **2004**, *108*, 2454–2463.
- (40) Smith, W.; Forester, T. R. *J. Mol. Graphics* **1996**, *14*, 136–141.
- (41) Hoover, W. G. *Phys. Rev. A* **1985**, *31*, 1695.
- (42) Berendsen, H. J. C.; Postma, J. P. M.; van Gunsteren, W. F.; DiNola, A.; Haak, J. R. *J. Chem. Phys.* **1984**, *81*, 3684–3690.
- (43) Mashl, R. J.; Scott, H. L.; Subramaniam, S.; Jakobsson, E. *Biophys. J.* **2001**, *81*, 3005–3015.
- (44) Tieleman, D. P.; Berendsen, H. J. C. *J. Chem. Phys.* **1996**, *105*, 4871–4880.
- (45) Patra, M.; Karttunen, M.; Hyvonen, M. T.; Falck, E.; Lindqvist, P.; Vattulainen, I. *Biophys. J.* **2003**, *84*, 3636–3645.
- (46) Simon, S. A.; McIntosh, T. J. *Proc. Natl. Acad. Sci. U.S.A.* **1989**, *86*, 9263–9267.
- (47) Gawrisch, K.; Ruston, D.; Zimmerberg, J.; Paresgian, V. A.; Rand, R. P.; Fuller, N. *Biophys. J.* **1992**, *61*, 1213–1223.
- (48) Flewelling, R. F.; Hubbell, W. L. *Biophys. J.* **1986**, *49*, 541–552.
- (49) Roux, B. *Comput. Phys. Commun.* **1995**, *91*, 275–282.
- (50) Kumar, S.; Rosenberg, J. M.; Bouzida, D.; Swendsen, R. H.; Kollman, P. A. *J. Comput. Chem.* **1995**, *16*, 1339–1350.
- (51) Grossfield, A. WHAM program: <http://dasher.wustl.edu/alan/>.
- (52) Lobaugh, J.; Voth, G. A. *J. Chem. Phys.* **1996**, *104*, 2056–2069.
- (53) Essmann, U.; Berkowitz, M. L. *Biophys. J.* **1999**, *76*, 2081–2089.
- (54) Moore, P. B.; Lopez, C. F.; Klein, M. L. *Biophys. J.* **2001**, *81*, 2484–2494.
- (55) Pfeiffer, W.; Henkel, T.; Sackmann, E.; Knoll, W.; Richter, D. *Europhys. Lett.* **1989**, *8*, 201–206.
- (56) Blume, A. In *Phospholipid Handbook*; Cevc, G., Ed.; Marcel Dekker: New York, 1993; pp 351–454.
- (57) Wyatt, D. L.; de Godoy, C. M. G.; Cukierman, S. *J. Phys. Chem. B* **2009**, *113*, 6725–6731.
- (58) Qin, Z.; Tepper, H. L.; Voth, G. A. *J. Phys. Chem. B* **2007**, *111*, 9931–9939.
- (59) Chernyshev, A.; Cukierman, S. *Biophys. J.* **2006**, *91*, 580–587.
- (60) Humphrey, W.; Dalke, A.; Schulten, K. *J. Mol. Graphics* **1996**, *14*, 33–38.
- (61) Barone, V.; Cossi, M. *J. Phys. Chem. A* **1998**, *102*, 1995–2001.
- (62) Breneman, C. M.; Wiberg, K. B. *J. Comput. Chem.* **1990**, *11*, 361–373.
- (63) Frisch, M. J.; Trucks, G. W.; Schlegel, H. B.; Scuseria, G. E.; Robb, M. A.; Cheeseman, J. R.; Montgomery, J. A., Jr.; Vreven, T.; Kudin, K. N.; Burant, J. C.; Millam, J. M.; Iyengar, S. S.; Tomasi, J.; Barone, V.; Mennucci, B.; Cossi, M.; Scalmani, G.; Rega, N.; Petersson, G. A.; Nakatsuji, H.; Hada, M.; Ehara, M.; Toyota, K.; Fukuda, R.; Hasegawa, J.; Ishida, M.; Nakajima, T.; Honda, Y.; Kitao, O.; Nakai, H.; Klene, M.; Li, X.; Knox, J. E.; Hratchian, H. P.; Cross, J. B.; Bakken, V.; Adamo, C.; Jaramillo, J.; Gomperts, R.; Stratmann, R. E.; Yazyev, O.; Austin, A. J.; Cammi, R.; Pomelli, C.; Ochterski, J. W.; Ayala, P. Y.; Morokuma, K.; Voth, G. A.; Salvador, P.; Dannenberg, J. J.; Zakrzewski, V. G.; Dapprich, S.; Daniels, A. D.; Strain, M. C.; Farkas, O.; Malick, D. K.; Rabuck, A. D.; Raghavachari, K.; Foresman, J. B.; Ortiz, J. V.; Cui, Q.; Baboul, A. G.; Clifford, S.; Cioslowski, J.; Stefanov, B. B.; Liu, G.; Liashenko, A.; Piskorz, P.; Komaromi, I.; Martin, R. L.; Fox, D. J.; Keith, T.; Al-Laham, M. A.; Peng, C. Y.; Nanayakkara, A.; Challacombe, M.; Gill, P. M. W.; Johnson, B.; Chen, W.; Wong, M. W.; Gonzalez, C.; Pople, J. A. *Gaussian 03*, Revision C.02; Gaussian, Inc.: Wallingford, CT, 2004.
- (64) Maupin, C. M.; Wong, K. F.; Soudackov, A. V.; Kim, S.; Voth, G. A. *J. Phys. Chem. A* **2006**, *110*, 631–639.
- (65) Lum, R. C.; Grabowski, J. J. *J. Am. Chem. Soc.* **1992**, *114*, 8619–8627.